Performance Test of an LSO-APD Detector in a 7-T MRI Scanner for Simultaneous PET/MRI

Bernd J. Pichler, PhD[1,2]; Martin S. Judenhofer, MS[1,2]; Ciprian Catana, MD[1]; Jeffrey H. Walton, PhD[3,4]; Manfred Kneilling, MD[5]; Robert E. Nutt, BS[6]; Stefan B. Siegel, PhD[6]; Claus D. Claussen, MD[2]; and Simon R. Cherry, PhD[1]

[1]Department of Biomedical Engineering, University of California, Davis, California; [2]Department of Radiology, Eberhard-Karls-University, Tuebingen, Germany; [3]Nuclear Magnetic Resonance Facility, University of California, Davis, California; [4]Biomedical Engineering Graduate Group, University of California, Davis, California; [5]Department of Dermatology, Eberhard-Karls-University, Tuebingen, Germany; and [6]Siemens Preclinical Solutions, Knoxville, Tennessee

PET combined with CT has proven to be a valuable multimodality imaging device revealing both functional and anatomic information. Although PET/CT has become completely integrated into routine clinical application and also has been used in small-animal imaging, CT provides only limited soft-tissue contrast and, in preclinical studies, exposes the animal to a relatively high radiation dose. Unlike CT, MRI provides good soft-tissue contrast even without application of contrast agents and, furthermore, does not require ionizing radiation. **Methods:** This project focused on combining a high-resolution PET scanner with a 7-T MRI system for animal research. Because classic PET detectors based on photomultiplier tubes cannot be used in high magnetic fields, we used a detector technology based on 10×10 lutetium oxyorthosilicate crystal arrays and 3×3 avalanche photodiode arrays. A ring of such PET detectors will ultimately be used as an insert for the 119-mm-diameter MRI bore. **Results:** Initial measurements with 1 PET detector module in the 7-T field during application of MRI sequences were encouraging. Position profiles from the PET detectors and a first MR image of a mouse could be acquired simultaneously. **Conclusion:** Further work will concentrate on the construction of a full PET detector ring with compact, integrated electronics.

Key Words: instrumentation; molecular imaging; PET; animal imaging; multimodality imaging; PET/MRI development

J Nucl Med 2006; 47:639–647

Nuclear imaging modalities such as PET or SPECT are distinguished from other functional in vivo imaging systems through their high sensitivity. Especially with PET, sensitivities in the picomolar range can be reached, providing quantitative in vivo information about functional processes such as glucose or amino-acid metabolism, receptor–ligand binding, or gene expression. However, PET generally provides limited anatomic information. For tracers and biomarkers with a high specificity or an unknown biodistribution, it is often difficult to determine exactly where they localize in vivo. This is a major drawback for high-resolution animal PET studies, especially in basic biomedical research applications such as cell-trafficking studies or new drug and tracer development. Although, in clinical applications, the combination of PET and CT scanners has already been established (*1–7*), many efforts are being made to combine high-resolution animal PET with dedicated CT systems to obtain anatomic information in preclinical studies (*8*). However, CT has low soft-tissue contrast and uses relatively high doses of ionizing radiation, which might have biologic effects on the animal models being studied (*9*). As an alternative, MRI can provide high spatial resolution and excellent soft-tissue contrast for anatomic imaging but suffers from poor signal strength, leading to low sensitivity for functional imaging. Thus, a combination of PET and MRI would be ideal for imaging in vivo functional processes and for providing advanced anatomic information with high soft-tissue contrast.

Standard PET detectors are based on photomultiplier tubes that read the light from scintillation crystals. Photomultiplier tubes are sensitive to magnetic fields even in the millitesla range. The magnetic field causes electrons to deviate from their original trajectory, resulting in a loss of gain. Thus, a combined PET/MRI scanner based on photomultiplier tube detectors can be realized only with optical fibers transporting the scintillation light outside the fringe magnetic field (*10,11*). Using long fibers to read the scintillation light causes several problems, such as light loss, resulting in degradation of energy and timing resolution. In addition, the more complicated design becomes impractical for a large number of detectors because of the large volume of fiber optics. Thus, the axial extent of the field of view of an optical fiber–based PET/MRI system will always be limited.

Avalanche photodiode (APD) technology has made big advances over the last few years (*12,13*). These compact and reliable silicon-based devices have successfully been used to replace bulky photomultiplier tubes in high-resolution

Received Aug. 17, 2005; revision accepted Dec. 23, 2005.

For correspondence or reprints contact: Bernd J. Pichler, PhD, Laboratory for Preclinical Imaging and Imaging Technology, Department of Radiology, University of Tuebingen, Roentgenweg 11, 72076 Tuebingen, Germany.

E-mail: Bernd.Pichler@med.uni-tuebingen.de

PET systems (*14,15*). APDs have been tested in high magnetic fields of up to 9.4 T (*16*) without showing any performance degradation. Hence, compact APD-based detectors offer new possibilities in merging PET and MRI.

Our group focuses on cell-trafficking research on small animals in the fields of oncology and immunology. Although microPET (Concorde Microsystems Inc.) scanners (*17,18*) provide exceptional temporal and functional information and a spatial resolution of approximately 1 mm in the reconstructed images, we see that a strong need for anatomic information still exists. High-resolution animal CT does not provide the required soft-tissue contrast for many applications and is coupled with a significant radiation dose of up to 0.1−1 Gy per scan (*19,20*). This is especially problematic in the field of immunology but also in longitudinal oncology studies (*21,22*). In addition, iodine-based contrast agents used in CT to enhance soft-tissue contrast are much more likely to cause biologic side effects than is any gadolinium-based MRI contrast agent (*23,24*).

Figure 1A shows an example of an in vivo cell-trafficking study; 10^6 tumor antigen (Tag)–specific Th1 cells were labeled in vitro with ^{64}Cu-pyruvaldehyde-bis(N4-methylthiosemicarbazone) (*25*) and transferred to transgenic RIP1-Tag2 mice (*26*) via intraperitoneal injection. Pancreatic tumors developed in the RIP1-Tag2 mice, and the goal of the study was to visualize Th1 cell trafficking for a new immunotherapy. The high-resolution PET revealed highly specific uptake (Fig. 1A) of labeled Th1 cells in the abdominal area, but the uptake locations could not be clearly assigned to a specific organ because of the lack of anatomic information.

In sharp contradistinction, Figure 1B shows an MR image of a mouse scanned in a 7-T tomograph (BioSpec; Bruker BioSpin) with application of a proton-weighted spin-echo sequence (Table 1). The MR image shows detailed anatomic structures with superior soft-tissue contrast although no contrast agents were administered.

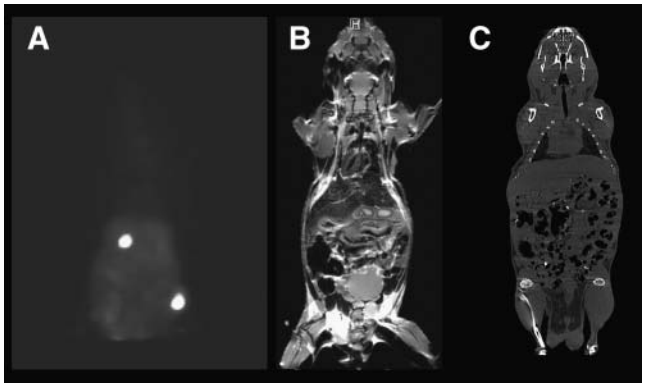

FIGURE 1. (A) Functional information at highest sensitivity is provided by PET images. (B) MRI provides superior anatomic information with excellent soft-tissue contrast. (C) High-resolution animal CT also provides good anatomic information but has poorer soft-tissue contrast and requires significant radiation dose.

TABLE 1
Parameters of Applied MRI Sequences

Sequence	Matrix	Pixel size (mm)	Recovery time (ms)	Echo time (ms)
Spin echo	128 × 128 or 256 × 256	0.6	2,415	22
Gradient echo	128 × 128 or 256 × 256	0.6	300	7.1

Figure 1C shows a CT image of a mouse without application of any contrast agent, resulting in a lower soft-tissue contrast than on the MR image (Fig. 1B). Thus, high-field MRI seems to be the ideal modality to supplement PET images with anatomic information.

For most circumstances in small-animal imaging, the accuracy of software-based image registration is unlikely to be sufficient for localization, especially in studies that focus on small lesions such as lymph nodes or that require long, dynamic PET scans to obtain temporal information about tracer distribution. The depth of breathing and the position of the animal change when an animal is kept under anesthesia for several hours. In addition, transferring an animal from one modality to another causes inaccuracies in animal positioning and adds anesthesia time.

Integrating a PET scanner into a high-field MRI scanner might also provide advanced in vivo spectroscopic information on tracer stability and binding. Furthermore, a positive side effect of operating a PET scanner inside an MRI scanner is that magnetic fields of more than 5 T have been shown to improve the spatial resolution of PET by reducing the mean free path of the positrons (*27*).

The goal of this project was to build a PET detector to fit inside the standard gradient set of a 7.05-T MRI scanner (BioSpec) (Fig. 2). Because the gradient set and the 35-mm mouse radiofrequency (RF) coil (Bruker BioSpin) are separated by only a 29-mm space, the PET detector needs to be compact. This requirement can easily be achieved by using an APD-based PET detector and integrated preamplifier electronics.

The main questions to be considered with this approach are whether APD-based PET detectors work reliably in a 7-T magnetic field while gradients and RF pulses are applied, whether shielding materials can be used to prevent electromagnetic fields from causing distortions and noise in the PET electronics, whether MRI is possible with a PET detector in the MRI scanner, and whether PET is possible with application of MRI pulse sequences.

MATERIALS AND METHODS

7-T MRI Tomograph

All studies were performed on a 7.05-T MRI tomograph (BioSpec) with a proton frequency of 300 MHz. The 7.05-T magnet was equipped with a gradient-coil system (Magnex Scientific). The gradient set had an inner diameter of 119 mm and provided a gradient strength of 95 mT/m at a maximum

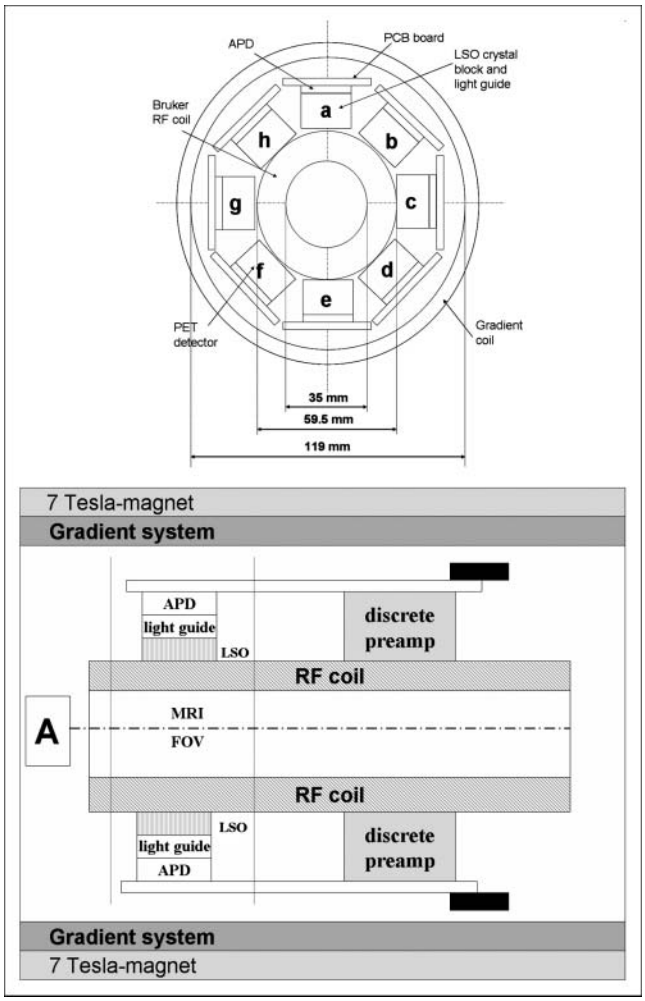

FIGURE 2. Top sketch shows ring consisting of compact LSO-APD detectors, which will be inserted into 7-T MRI scanner. PET detector will be mounted between RF and gradient coils to allow simultaneous PET/MRI. Bottom sketch shows longitudinal (axial) section through MRI scanner and PET insert. FOV = field of view; PCB = printed circuit board.

current of 200 A. For MRI data acquisition, image display, and data analysis, the ParaVision software platform (Bruker BioSpin) was used. Standard MRI spin-echo and gradient-echo sequences provided by the ParaVision software were used for the tests. Table 1 describes these sequences and shows the chosen values for recovery time, echo time, and pixel size. The chosen matrix size was either 128×128 or 256×256. The gradient echo used a 30° tip angle. A 35-mm-diameter RF probe coil (Bruker BioSpin) was tuned and matched to its optimum. The gradient coils were shimmed by using the automatic shimming tool provided by the ParaVision software.

As a phantom, a glass sphere 30 mm in diameter and filled with 150 mmol of NaCl was used.

PET Detector Setup

A monolithic 3×3 APD array (Hamamatsu Photonics) (*13*) was connected to 9 charge-sensitive preamplifiers (Max-Planck-Institute for Physics) (*28*). The individual APDs of the array had an active surface of 5×5 mm and an internal gain of approximately 100 at a bias voltage of approximately 360 V. The dark current was approximately 10 nA per APD. The high voltage was supplied by a low-noise power supply (series 230; Bertan) placed outside the 5-G fringe field. The hybrid charge-sensitive preamplifier (*28*) had a gain of 0.5 μV/electron, a signal rise time of 20 ns, and a noise of 560 electrons + 17 electrons/pF noise slope (50-ns integration time). The APD array and the preamplifiers were mounted on a standard printed circuit board, with the APD array approximately 60 mm away from the preamplifiers (Fig. 3). The high voltage and the ±12-V direct-current preamplifier power were supplied and the amplifier signals were read by 4-m-long nonmagnetic 50-Ω coaxial cables.

Determination of Frequency Line Width for Different Materials

The 29-mm distance between the RF and gradient coil provides enough space for the future lutetium oxyorthosilicate (LSO)-APD PET detector (Fig. 2). The most important detector materials (APD array, LSO crystal block, and electronics) were placed outside the RF coil, and the frequency line widths for the different materials were determined to detect their potential influences on the homogeneity of the magnetic field. Thus, materials influencing the homogeneity of the magnetic field would broaden the frequency line width. The ParaVision software provides an automated routine for determining the frequency line widths.

Basic Tests with LSO-APD PET Detector in Magnet

For energy spectrum acquisitions, a single $2 \times 2 \times 6$ mm LSO scintillation crystal (CTI Inc.) was wrapped in 6 layers of Teflon (DuPont) tape and coupled by optical grease (BC-630; Bicron) to the center APD of the array. The reason for using a single crystal rather than an LSO crystal block, as in the final detector design, is that an analysis of spectra derived from a single crystal is much

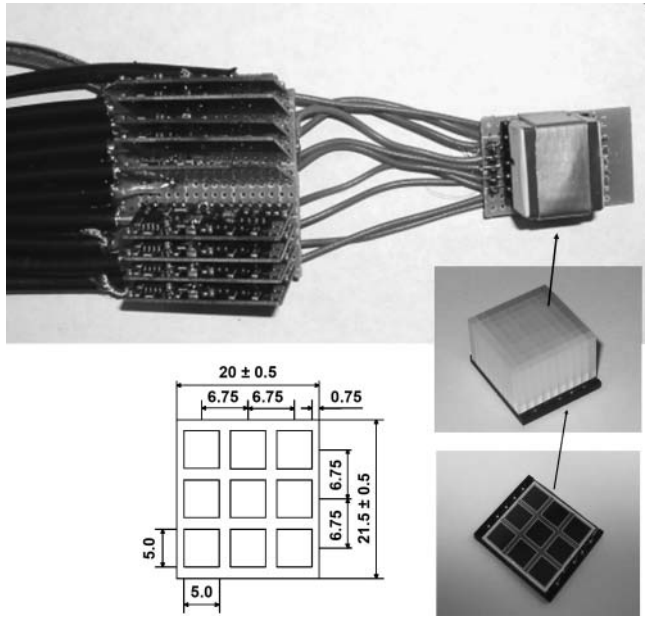

FIGURE 3. LSO-APD detector assembly: 10×10 LSO array (center right) was coupled by custom-made light guide to 3×3 APD array (bottom right). Signals were read by 9 hybrid charge-sensitive preamplifiers (top). Nonmagnetic 50-Ω coaxial cables were used to channel signals out of magnet. Sketch shows dimensions (in mm) of 3×3 APD array.

more accurate. Thus, even minimal deviations in energy resolution, 511-keV peak position, or the ratio of Compton events to photo effect can much more easily be detected.

For energy spectra acquisitions with the single LSO crystal, an approximately 3,700-kBq ^{22}Na source was used (Isotope Products). The analog APD signals were amplified by the preamplifier and shaped (500-ns integration time) with a 579-filter amplifier (Ortec) before being digitized with a multichannel analyzer (MCA 8000A; Amptek). Energy resolution and peak position (511 keV) were analyzed with the MCA 8000A software package. All electronics except the detector and preamplifier were placed outside the fringe magnetic field.

To ensure stable operation of the sensitive PET detector electronics without oscillations or excess noise, electrical shielding is important. For the basic tests of the APD detector with the single LSO crystal, we used a standard electronics aluminum enclosure approximately 3 mm thick—usually applied for sensitive electronics circuits—that fit in the bore of the 7-T magnet. However, because the aluminum housing for the entire PET detector was too large to fit inside the RF coil, the detector was positioned inside the gradient coil of the 7-T MRI scanner but in front of the RF coil (position is indicated with an "A" in Fig. 2). Thus, the PET detector was not in the same position as it would be in the final system.

Energy spectra were acquired with this assembly outside the magnetic field, inside the MRI scanner, and while applying gradient and spin-echo sequences to encounter potential effects of the MRI system on PET detector performance.

Optimization of PET Detector Shielding

The APD array and charge-sensitive preamplifiers in the final setup need to be shielded to avoid electronic oscillations, or signal pickup, and to reduce noise caused by RF signals, gradient switching, or other external sources. High-frequency electronics are usually shielded with aluminum or copper enclosures connected to a ground. For the final PET detector insert, the LSO-APD modules will be arranged radially around the RF coil. To optimize shielding, we placed the PET detectors and amplifiers between 2 concentric metal cans having a lid on both ends. As material, we considered using copper, brass, or aluminum. Because copper is easy to machine, nonmagnetic, nonferromagnetic, and known to be a good electrical shielding material, the 2 concentric metal cans were based on copper with 99% purity to minimize ferromagnetic contamination. The first prototype had a material thickness of 0.8 mm to optimize mechanical stability and shielding. The second prototype had only a 0.15-mm material thickness. To reduce potential eddy currents induced by the gradients, we made an axial slit in each of the 2 cans.

The RF coil was placed inside the smaller can, and the assembly was inserted into the MRI scanner. To detect potential effects on MR image quality, we scanned the NaCl-filled phantom and determined the signal-to-noise ratio (SNR) with the ParaVision software by placing a region of interest (~1.5 cm in diameter) in the reconstructed MR image inside the phantom and at the background outside the phantom.

Acquisition of PET Position Profiles While Applying MRI Sequences

Position profiles were acquired with a 10 × 10 LSO block having a crystal size of 2 × 2 × 12 mm (*13*). The crystal block was coupled by a custom-made 3.5-mm-thick acrylic light guide (*13*) and optical grease to the APD array. All energy spectra and position profiles were acquired with a sealed ^{22}Na disk source of approximately 3,700 kBq (Isotope Products). The 9 APD signals were first shaped (integration time, 150 ns) with a custom-made 9-channel shaping amplifier board, followed by a 200-ns integration applied by a N568 spectroscopy amplifier board (CAEN). The shaped signals were simultaneously digitized by a PD2MFS-C-UT data acquisition board (United Electronics Industries, Inc.). A trigger signal had to be generated to initiate a conversion start signal for the data acquisition board (*29*). This trigger signal was derived by summing all 9 preamplified nonshaped APD signals by a dedicated fast summing circuit board and feeding its output into a constant fraction discriminator (TC-435; Tennelec). Again, all electronics beyond the preamplifier were located outside the fringe magnetic field. The LSO-APD detector including the 9 preamplifiers was built between the 2 copper cans and placed with the RF coil inside the MRI scanner as described before. The setup of the LSO-APD PET detector was optimized for RF shielding and analog ground distribution. In addition, we took care that the main components were nonmagnetic, although this was not the case for some of the surface-mount devices such as capacitors or resistors on the preamplifier board. Position profiles were acquired with the PET detector and shielding cans in the MRI scanner before and during MRI of the NaCl phantom. Spin-echo and gradient-echo imaging sequences were used (Table 1). The noise levels of the PET detector and the SNR from the MR image were analyzed. The position profiles were analyzed by a custom software tool (*29*), and profiles through the MR images were drawn with the ParaVision software tool, revealing inhomogeneities in the images.

Phantom Imaging to Determine SNR from LSO and APD Array

Although the studies described in the previous section were performed with electronics boards consisting of some magnetic parts (capacitors and resistors) and copper cans shielding the electronics, we further investigated the influence on the MR images of the 2 most important parts of the PET detector: the APD array and LSO block itself. The APD array and LSO block were placed around the RF coil with no shielding, and the NaCl phantom was again imaged with spin-echo and gradient-echo sequences. The SNR was analyzed in the reconstructed images. In contrast to the frequency line width, these measurements indicated potential effects of the materials on the gradients.

RESULTS

Determination of Frequency Line Width for Different Materials

Basic measurements concentrated on the influence of essential detector materials—such as the LSO crystal block, APD array, printed circuit board, and amplifier—on MRI, specifically on MRI field homogeneity and RF effects. The PET detector materials were placed outside the RF coil, and the frequency line width was determined. The frequency line width was 24 Hz without any materials and for all materials placed in the scanner. Thus, no significant changes in frequency line width were observed, indicating that the chosen PET detector materials might not affect MRI field homogeneity.

Basic Tests with LSO-APD PET Detector in Magnet

The measurements with a single LSO crystal coupled to the center APD of the array are summarized in Table 2. For this test, the APD and preamplifier were placed in an aluminum box, achieving good shielding for the PET electronics. Different MRI sequences were applied, and the 511-keV peak position and 511-keV energy resolution (full width at half maximum) were determined (Table 2) in order to reveal potential effects of the MRI sequences on PET detector performance. Figure 4 shows a representative energy spectrum from a ^{22}Na source, acquired with the LSO-APD detector while a spin-echo sequence was applied. The data are represented as mean $\pm$ σ ($n = 3$). Although the energy resolution was best (14.0%) when the detector was placed outside the MRI scanner, it degraded only slightly inside the scanner (14.6%). Energy resolution degraded when MRI sequences were applied (18.2% and 18.7% for gradient echo and spin echo, respectively). This degradation was caused by noise picked up from the MRI gradients and RF pulses. An energy resolution in this range is still acceptable for PET, but there are ways to improve the range by shielding and ground distribution. More important, the peak position did not change significantly for the different tests.

Optimization of PET Detector Shielding

Basic tests using sheets of copper, brass, and aluminum in the MRI scanner while applying spin-echo sequences showed that copper influenced MR images the least. Two concentric copper cans—one having a material thickness of 0.8 mm and the other having a material thickness of 0.15 mm—were built. Although MRI with the 0.8-mm copper cans surrounding the RF coil was impossible (Fig. 5B), MRI of the NaCl phantom with 0.15-mm copper was feasible (Fig. 5C). However, the images revealed an approximately 30% reduction in SNR (from 43 to 30), compared with the same phantom imaged without the copper shielding (Fig. 5A). This loss of signal was most probably caused by increased eddy currents in the thicker material. The chosen imaging protocol was based on a spin-echo sequence with a 128 $\times$ 128 matrix and the parameters shown in Table 1. For these measurements and the tests in the next sections, the setup shown in Figure 6 was used.

TABLE 2
Acquisition of Energy Spectra with LSO-APD Detector

PET detector location	Applied sequence	511-keV peak position (norm.)	511-keV energy resolution (%)
Outside 5-G field	NA	1.0	14.0 $\pm$ 0.2
Inside MRI scanner	NA	1.1	14.6 $\pm$ 0.3
Inside MRI scanner	Shimming	1.0	15.3 $\pm$ 0.3
Inside MRI scanner	Gradient echo	1.0	18.2 $\pm$ 1.5
Inside MRI scanner	Spin echo	1.0	18.7 $\pm$ 1.8

norm. = normalized; NA = not applicable.

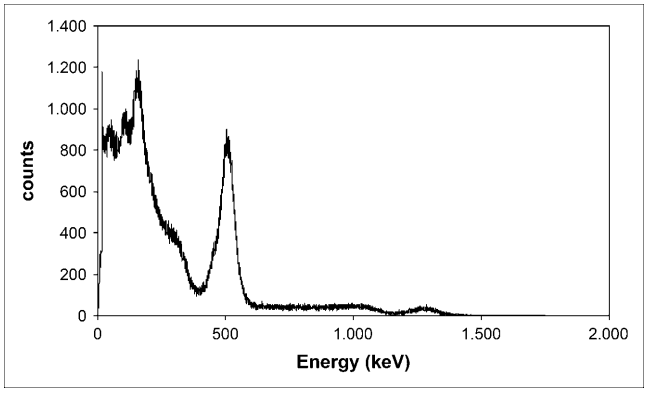

FIGURE 4. Representative 511-keV energy spectrum acquired with LSO-APD detector in 7-T MRI scanner while applying spin-echo sequence. Energy resolution was 18.7% (511 keV, full width at half maximum). Although energy resolution is still good and linearity is maintained between the two ^{22}Na peaks, MRI sequence causes increased noise in low-energy region.

Acquisition of PET Position Profiles While Applying MRI Sequences

On the basis of the encouraging results with the single LSO crystal coupled to the APD detector and operated in the MRI scanner while applying imaging sequences, we performed further tests with the LSO crystal block and the APD array. Figure 7A shows the position profile of the LSO-APD detector acquired outside the MRI scanner. The PET detector electronics were shielded by the 2 copper cans (0.15-mm material thickness) as described. A total of 64 individual crystals (8 rows and 8 columns) from the 10 $\times$ 10 LSO block could be separated in the position profiles. The outer 2 rows of the block could not be separated, most likely because the positioning of the light guide and LSO array was not accurate enough in this prototype setup. Nevertheless, the same setup was used in combination with the RF coil and the NaCl phantom inside the MRI scanner (Fig. 6). Position profiles were acquired while the setup was in the MRI scanner (Fig. 7B) and while applying the spin-echo imaging sequence (Table 1). The resulting position profiles are shown in Figure 7C. Although the position profiles acquired in the MRI scanner look noisier than the one acquired outside the MRI scanner, all 64 crystals could be separated clearly. The additional noise might be reduced by a proper setup based on a multilayer printed circuit board, better signal shaping, and optimized grounding and shielding. The oscilloscope picture in Figure 7C shows increased baseline noise caused by the applied MRI sequence. However, this effect does not influence the position profile (Fig. 7C). Although acquiring the position profiles,

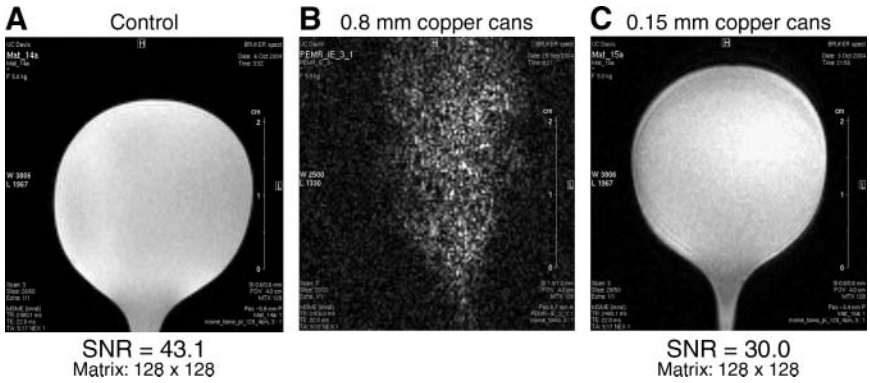

FIGURE 5. (A) NaCl-filled spheric phantom imaged with spin-echo sequence when no parts of PET detector or shielding materials were in MRI scanner. Measured SNR is 43.1. (B) When mouse was scanned with two 0.8-mm-thick copper cans in field of view of magnet, almost no signal could be measured. (C) SNR of 30.0 is obtained using copper cans with 0.15-mm material thickness.

the NaCl phantom was imaged with the spin-echo sequence. The reconstructed MR image of the NaCl phantom is shown in Figure 8 and reveals a significantly reduced SNR—by a factor of 10 compared with the control measurement (Fig. 5A)—and a 50% inhomogeneity in signal amplitude. As a general proof of principle, a first MR image of a dead mouse was obtained while the PET detector was in the MRI scanner and acquiring data. Although the image of the mouse was reduced in quality, anatomic details could be detected clearly and might already provide sufficient morphologic information for many imaging studies.

Phantom Imaging to Determine SNR from LSO and APD Array

The measurements described in Figure 8 showed a significant reduction of SNR in the MR image. Because the measurements of the frequency line width revealed no broadening of the frequency line, the reduction of SNR was likely not caused by the RF but by the gradients. Because we had few resistors and capacitors on our electronics board showing residual magnetism, which might interfere with the gradients, it was important to test the parts essential for building a detector unit. The main components of the detector are the LSO block and the APD array, both of which are nonmagnetic. For all other parts, such as resistors or capacitors, we found nonmagnetic alternatives. However, we placed the LSO block and APD array around the RF coil and inserted the setup, including the NaCl spheric phantom, inside the MRI scanner. As the imaging sequence, we used spin echo as described in Table 1. The reconstructed MR image of the NaCl phantom is shown in Figure 9; no significant artifacts were visible and the profiles revealed signal homogeneity of more than approximately 90%. Because the SNR was comparable to the control measurement (Fig. 5), the reduction of SNR was likely caused only by interference of the gradients with parts of the magnetic surface-mount device on the electronics board.

In this experiment, the electronics were completely removed. To exclude the possibility that the interference arose from powered-on PET electronics, we repeated the tests shown in Figure 8 with powered-off electronics, but we saw no significant improvements.

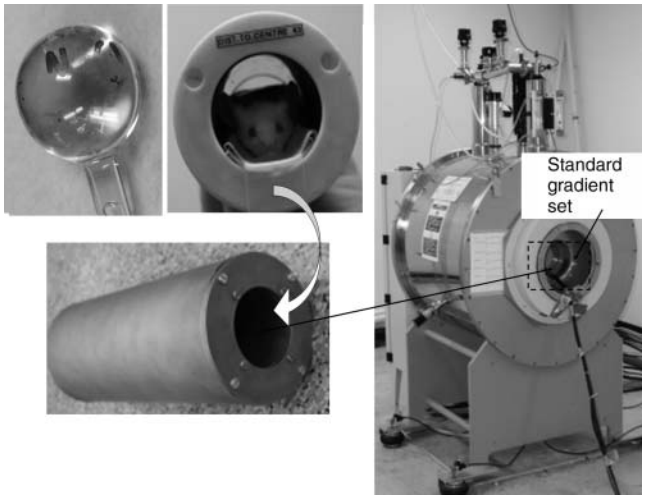

FIGURE 6. Experimental setup consists of NaCl phantom (top left), RF coil (top center, with mouse), 7-T BioSpec (Bruker BioSpin) MRI scanner (right), and copper can that serves as detector shielding (bottom left).

DISCUSSION

Basic measurements with and without placement of major detector components inside the gradient set revealed no change in the frequency line width, indicating that the detector components did not interfere with the RF pulses or the main magnetic field of the scanner. Furthermore, images acquired of a NaCl-filled phantom while the LSO block and the APD array were placed around the RF coil showed no degradation or artifacts (Fig. 9).

The acquired PET-detector energy spectra (Table 2) show only slight degradation caused by gradients or RF pulses. Optimized shielding might further reduce or even completely remove this interference.

Measurements with the entire APD and preamplifier electronics chain showed that optimized electronics shielding is vital to maintaining the quality of the low-amplitude APD signals. Copper seems to be the best shielding

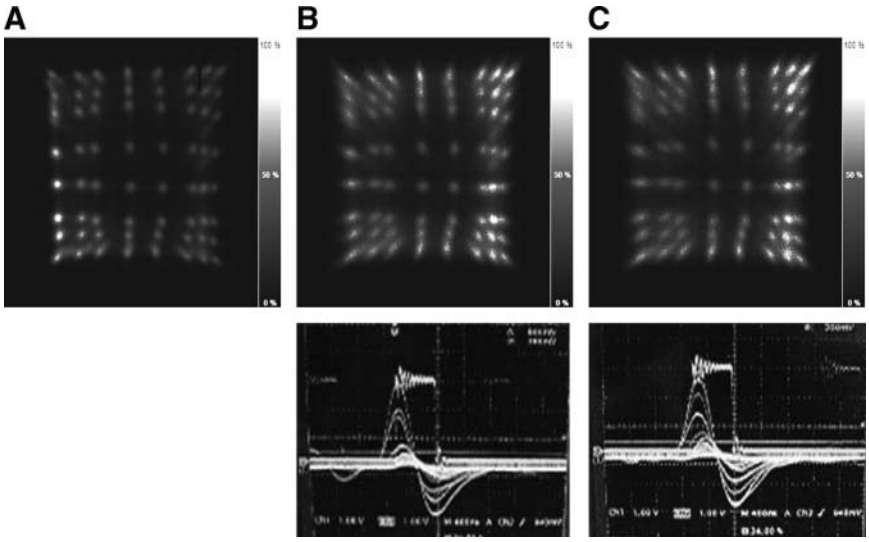

FIGURE 7. Acquisition of position profile with LSO-APD detector outside 7-T magnet (A), inside magnet (B), and during MRI with spin-echo sequence (C). Corresponding analog signals after 200-ns shaping are shown below for detector in magnet (B) and while applying spin-echo sequence (C). Signal baseline shows slightly increased noise level (oscilloscope pictures) when spin-echo sequence is applied. Square signal in oscilloscope diagram shows trigger that initiates sampling for analog–digital conversion.

material for electronics circuits, but its thickness influences MR image quality. Although MRI was impossible with a 0.8-mm-thick copper shield, reducing the thickness to 0.15 mm allowed the acquisition of reasonable MR images (Fig. 5). The SNR in that case was reduced by only 30%, compared with the SNR of images acquired without any shielding in the MRI scanner. More advanced shielding designs might lead to an improved SNR for MRI.

Importantly, neither the performance of the APD array nor that of the preamplifier electronics was destroyed or degraded by application of gradients and different RF pulse sequences. Tests performed over several days detected no degradation of APD or electronics performance.

Although the simultaneously acquired position profiles from the PET detector (Fig. 7) and the MR images (Fig. 8) provide room for improvement, they clearly demonstrate the feasibility of a combined PET/MRI system for simultaneous imaging of function and morphology.

In contrast to other proposed PET/MRI scanners (*10,11,30*), our approach with APD-based detectors is not limited in the axial field of view and will preserve a good energy and timing resolution because no optical fibers are involved.

CONCLUSION

We have shown for, what is to our knowledge, the first time that simultaneous acquisition of PET data during MRI is possible with an APD-based PET detector built into a 7-T MRI scanner. We performed all our studies on a

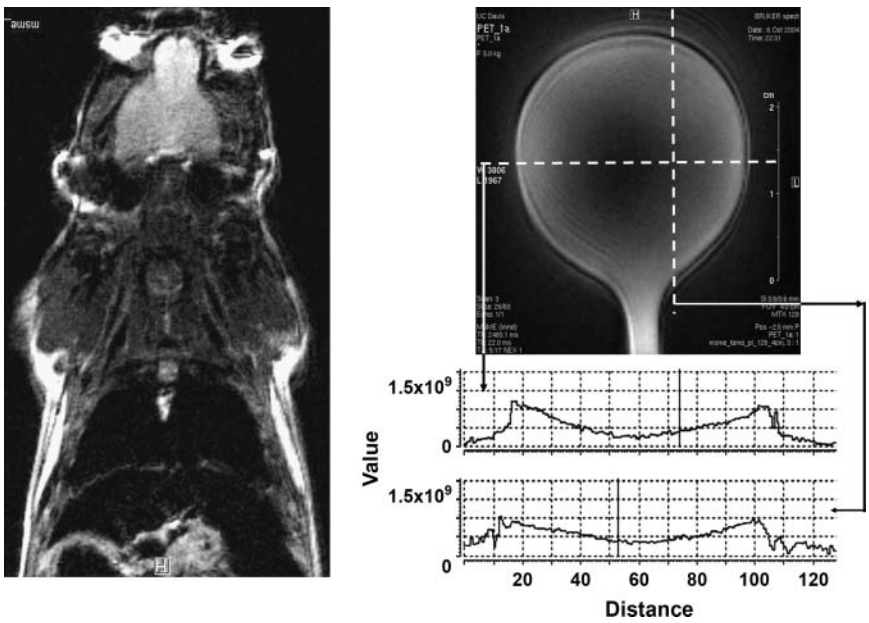

FIGURE 8. On left is MR image acquired with spin-echo sequence during which PET detector was also in MRI scanner acquiring position profiles. Although anatomic details of mouse are visible, SNR is obviously worse than in image shown in Figure 1B. On right is MR image of NaCl phantom and corresponding profiles through phantom. SNR was only 3.4.

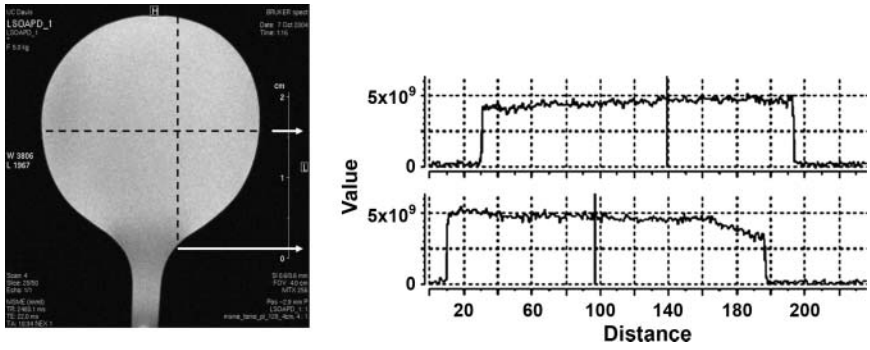

FIGURE 9. MRI of NaCl spheric phantom during application of spin-echo sequence with LSO and APD array in field but with no electronics in place. SNR of phantom was about 45. Corresponding profiles demonstrate good homogeneity.

7-T magnet dedicated for research on small animals. However, we believe that the results are translatable to clinical MRI scanners that have a magnetic field 2- to 5-fold lower.

A combined PET/MRI system could be made even more powerful if nuclear spectroscopy were to be applied at the same time during PET. This would open new possibilities for tracer evaluation in vivo.

The 7-T magnetic field would also shorten the mean free path of the positron range (*27*); thus, image quality, especially in the field of small-animal imaging, might improve significantly.

For further integration, we are working on a board layout housing an integrated charge-sensitive preamplifier (*13*) and the APD array. Several detector modules will be arranged in a ring fitting into the 7-T magnet bore, as shown in Figure 2, for further evaluation.

ACKNOWLEDGMENTS

This work was supported by grants EB004483 and EB000993 from the NIBIB-NIH and by the 2004 NMR Award from the University of California, Davis. Dr. Kuei Yamamoto, Hamamatsu Photonics, Japan, supported this work generously by providing APD arrays. We thank Dr. Eckart Lorenz and Wendelin Pimpl, Max-Planck-Institute for Physics, Munich, Germany, for providing the charge-sensitive preamplifiers. Also, we thank Earl Hegert and Ed Baro, Hamamatsu Photonics, USA, for their interest in and support of this work, and we thank Jane Gollub for proofreading the manuscript. Dr. Julie Sutcliffe-Goulden and David Kukis, University of California, Davis, provided ^{64}Cu-pyruvaldehyde-bis(N4-methylthiosemicarbazone) for the PET image shown in the introduction.

REFERENCES

1. Akhurst T, Chisin R. Hybrid PET/CT machines: optimized PET machines for the new millennium? *J Nucl Med.* 2000;41:961–963.
2. Beyer T, Townsend DW, Brun T, et al. A combined PET/CT scanner for clinical oncology. *J Nucl Med.* 2000;41:1369–1379.
3. Beyer T, Townsend DW, Blodgett TM. Dual-modality PET/CT tomography for clinical oncology. *Q J Nucl Med.* 2002;46:24–34.
4. Ell PJ, von Schulthess GK. PET/CT: a new road map. *Eur J Nucl Med Mol Imaging.* 2002;29:719–720.
5. Townsend DW. A combined PET/CT scanner: the choices. *J Nucl Med.* 2001; 42:533–534.
6. Townsend DW, Beyer T. A combined PET/CT scanner: the path to true image fusion. *Br J Radiol.* 2002;75 Spec No:S24–S30.
7. Townsend DW, Beyer T, Blodgett TM. PET/CT scanners: a hardware approach to image fusion. *Semin Nucl Med.* 2003;33:193–204.
8. Jan ML, Chuang KS, Chen GW, et al. A three-dimensional registration method for automated fusion of micro PET-CT-SPECT whole-body images. *IEEE Trans Med Imaging.* 2005;24:886–893.
9. Boone JM, Velazquez O, Cherry SR. Small-animal x-ray dose from micro-CT. *Mol Imaging.* 2004;3:149–158.
10. Shao Y, Cherry SR, Farahani K, et al. Development of a PET detector system compatible with MRI/NMR systems. *IEEE Trans Nucl Sci.* 1997;44: 1167–1171.
11. Yamamoto S, Kuroda K, Senda M. Scintillator selection for MR compatible gamma detectors. In: *2002 IEEE Nuclear Science Symposium Conference Record.* Piscataway, NJ: IEEE; 2002.
12. Dokhale PA, Silverman RW, Shah KS, et al. Performance measurements of a depth-encoding PET detector module based on position-sensitive avalanche photodiode read-out. *Phys Med Biol.* 2004;49:4293–4304.
13. Pichler BJ, Swann BK, Rochelle J, Nutt RE, Cherry SR, Siegel SB. Lutetium oxyorthosilicate block detector readout by avalanche photodiode arrays for high resolution animal PET. *Phys Med Biol.* 2004;49:4305–4319.
14. Ziegler SI, Pichler BJ, Boening G, et al. A prototype high-resolution animal positron tomograph with avalanche photodiode arrays and LSO crystals. *Eur J Nucl Med.* 2001;28:136–143.
15. Lecomte R, Cadorette J, Rodrigue S, et al. Initial results from the Sherbrooke avalanche photodiode positron tomograph. *IEEE Trans Nucl Sci.* 1996;43: 1952–1957.
16. Pichler B, Lorenz E, Mirzoyan R, et al. Performance test of a LSO-APD PET module in a 9.4 Tesla magnet. In: *Conference Record of the 1998 IEEE Nuclear Science Symposium and Medical Imaging Conference.* Piscataway, NJ: IEEE; 1998:1237–1239.
17. Tai YC, Ruangma A, Rowland D, et al. Performance evaluation of the microPET Focus: a third-generation microPET scanner dedicated to animal imaging. *J Nucl Med.* 2005;46:455–463.
18. Yang Y, Tai YC, Siegel S, et al. Optimization and performance evaluation of the microPET II scanner for in vivo small-animal imaging. *Phys Med Biol.* 2004; 49:2527–2545.
19. Weissleder R. Scaling down imaging: molecular mapping of cancer in mice. *Nat Rev Cancer.* 2002;2:11–18.
20. Paulus MJ, Gleason SS, Kennel SJ, Hunsicker PR, Johnson DK. High resolution x-ray computed tomography: an emerging tool for small animal cancer research. *Neoplasia.* 2000;2:62–70.
21. Liu XD, Ma SM, Liu SZ. Effects of 0.075 Gy x-ray irradiation on the expression of IL-10 and IL-12 in mice. *Phys Med Biol.* 2003;48:2041–2049.
22. Mahnke YD, Schirrmacher V. A novel tumour model system for the study of long-term protective immunity and immune T cell memory. *Cell Immunol.* 2003; 221:89–99.
23. Piironen A. Severe acute pancreatitis: contrast-enhanced CT and MRI features. *Abdom Imaging.* 2001;26:225–233.
24. Werner J, Schmidt J, Warshaw AL, Gebhard MM, Herfarth C, Klar E. The relative safety of MRI contrast agent in acute necrotizing pancreatitis. *Ann Surg.* 1998;227:105–111.

25. Adonai N, Nguyen KN, Walsh J, et al. Ex vivo cell labeling with ^{64}Cu-pyruvaldehyde-bis (N4-methylthiosemicarbazone) for imaging cell trafficking in mice with positron-emission tomography. *Proc Natl Acad Sci U S A.* 2002;99:3030–3035.
26. Hanahan D. Heritable formation of pancreatic beta-cell tumours in transgenic mice expressing recombinant insulin/simian virus 40 oncogenes. *Nature.* 1985; 315:115–122.
27. Hammer BE, Christensen NL, Heil BG. Use of a magnetic field to increase the spatial resolution of positron emission tomography. *Med Phys.* 1994;21:1917–1920.
28. Pichler BJ, Boening G, Lorenz E, et al. Studies with a prototype high resolution PET scanner based on LSO-APD modules. *IEEE Trans Nucl Sci.* 1998;45:1298–1302.
29. Judenhofer MS, Pichler BJ, Cherry SR. Evaluation of high performance data acquisition boards for simultaneous sampling of fast signals from PET detectors. *Phys Med Biol.* 2005;50:29–44.
30. Marsden PK, Strul D, Keevil SF, Williams SC, Cash D. Simultaneous PET and NMR. *Br J Radiol.* 2002;75 Spec No:S35–S39.